Performance enhancement of mesoporous TiO_2-based perovskite solar cells by SbI_3 interfacial modification layer

Putao Zhang, Fu Yang, Muhammad Akmal Kamarudin, Chi Huey Ng, Gaurav Kapil, Tingli Ma,

Shuzi Hayase*

Graduate School of Life Science and Systems Engineering, Kyushu Institute of Technology, 2-4

Hibikino, Wakamatsu-ku, Kitakyushu, Fukuoka 808-0196, Japan

*Corresponding author: hayase@life.kyutech.ac.jp

Abstract: TiO_2 is commonly used as the electron transporting material in perovskite photovoltaic devices due to its advantages, including suitable band gap, good photoelectrochemical stability, and simple preparation process. However, there are many oxygen vacancies or defects on the surface of TiO_2 and thus this affects the stability of TiO_2 based perovskite solar cells under UV light. In this work, a thin (monolayer) SbI_3 modification layer is introduced on the mesoporous TiO_2 surface and the effect at the interface between of TiO_2 and perovskite is monitored by using a quartz crystal microbalance system. We demonstrate that the SbI_3-modified TiO_2 electrodes exhibit superior electronic properties by reducing electronic trap states, enabling faster electron transport. This approach results in higher performances compared with that without SbI_3 passivation layer electrodes. $CH_3NH_3PbI_3$ perovskite solar cells with a maximum power conversion efficiency of 17.33% in air, accompanied by a reduction in hysteresis and enhancement of the device stability are reported.

Keywords: perovskite solar cells, electron transport layer, interface, SbI_3, passivation

Introduction

Perovskite solar cells (PSCs) have gained considerable attention in the recent years due to their unique optoelectronic properties such as tunable band gap in the visible range, high absorption coefficient, high charge carrier mobility, long charge carrier lifetime and large charge carrier diffusion length [1-4]. For these reasons, the power conversion efficiency (PCE) of PSCs has been improved tremendously from initially 3.8% to over 22.7% within the past few years by optimizing the solar cell structures and perovskite film deposition methods, tuning perovskite compositions, improving interface quality or reducing interface defects[5-6]. The high efficiency is almost approaching that of commercial silicon solar cells or other inorganic thin film solar cells such as copper indium gallium selenide (CIGS) and cadmium telluride (CdTe) solar cells. Although PSCs have achieved impressive PCE values, some key issues such as long-term stability, hysteresis behavior and cost of production still exist in the generally fabricated PSCs. The decay of device performance in ambient air condition is a great hurdle for the

commercialization of PSCs. The phenomenon of hysteresis in PSCs is caused by interface defects, ion migration or ferroelectric effect etc.[7-8]. In order to improve the performance of PSCs, the hysteresis issue needs to be resolved to ensure a reliable performance.

In the perovskite photovoltaic devices, cells with mesoporous structure (Cell 1)[9] and that with planar structures (Cell 2)[10] have been reported. Cell 1 has semiconductor or insulator nanoparticles as a scaffold layer. There is a large number of voids in the scaffold layer. The perovskite precursor solution can easily penetrate into the interstices of the scaffold layer and finally forms a continuous perovskite layer in the interface of the scaffold layer. Cell 2 does not need the mesoporous layer and form a sandwich structure with the p-type and n-type semiconductor. In addition, there are some new structures such as inverted structure, a hole transporting layer free structure, an electron transporting layer free structure. In all of these structures, a device with mesoporous structure has the best repeatability and the highest solar cell efficiency so far [6]. In Cell 1, researchers modified the electron transport layer in various ways in order to get more excellent performance. In the case of mesoporous TiO_2 (mp-TiO_2) based PSCs, a variety of dopants has been investigated, including Al[11], Co[12], Li[13-15], Mg[16], K[17], Ru[18], Nb[19], Y[20], and other additives[21]. Various interfacial modifiers have also been studied including organic molecules [22-23], metal oxides[24] other materials[25-26]. However, little attention has been paid to the passivation of TiO_2 by SbI_3 and how it binds to TiO_2.

In this work, we adopted a simple immersion method to form a SbI_3 passivation layer on the surface of TiO_2. Quartz crystal microbalance system (QCM) was used to monitor the binding of SbI_3 molecules to TiO_2 surface groups. It has been shown that SbI_3 monolayer on TiO_2 surface can be formed utilizing the simple immersion of the TiO_2 substrate, which not only reduces TiO_2 surface defects but also improves the morphology of the $CH_3NH_3PbI_3$ perovskite film. The results show that hysteresis is significantly reduced, and the long-term stability in the air environment is greatly improved after the SbI_3 passivation. A high device performance of 17.33% (16.41%, average) and enhanced device stability was achieved, compared to those of devices without the passivation (champion 15.82%, average 15.04%).

Experiment section

Materials. Unless specified otherwise, all materials were purchased from either Wako Pure Chemical Industries, Ltd. or Tokyo Chemical Industry Co., Ltd. and used as received without further purification.

Device fabrication. Firstly, fluorine-doped tin oxide (FTO) glass (Nippon Sheet Glass Co. Ltd.) was cut into pieces with dimensions of 20 mm × 20 mm and etched with zinc powder and hydrochloric acid solution (6 M). Then the substrates were washed with detergent, acetone, isopropanol and deionized water for 15 min, respectively under ultrasonic condition. Then the substrates were dried with air and treated with oxygen plasma for 10 min. To prepare a TiO_2 compact layer (c-TiO_2), 0.15 M titanium diisopropoxide bis (acetylacetonate) (75 wt% in isopropanol, Sigma-Aldrich) in 1-butanol (99.8%, Sigma-Aldrich) solution was spin-coated on an FTO substrate at 2000 rpm for 20 s, which was followed by heating on a hotplate at 125 °C for 5 min[27] (thickness of the c-TiO_2 is ~40 nm, see Fig. S1 in supporting information). After cooling down to room temperature, the diluted-TiO_2 paste was spin-coated on the c-TiO_2 layer at

5000 rpm for 30 s, where the paste was diluted in ethanol (TiO_2 paste/ethanol = 1/ 4, weight ratio). After drying on the hotplate at 125 °C for 5 min, the film was annealed at 500 °C for 1 h, providing a mesoporous TiO_2 (mp-TiO_2) with a thickness of 150~200 nm (~165 nm in average, see Fig. S2). The SbI_3 passivation layer was then introduced on the mp-TiO_2 surface by immersion the substrates into a 0.2 mM of SbI_3/DMF solution for 30 min, followed by rinsing the film with DMF solution and then drying with air. Light harvesting layer, $CH_3NH_3PbI_3$, was prepared using the one-step anti-solvent method. 1.5 M of perovskite precursor solution was prepared by using methylammonium iodide (MAI, 477 mg) and lead iodide (PbI_2, 1452 mg) dissolved in a binary solution of N, N-dimethylformamide (DMF, 1.6 mL) and dimethyl sulfoxide (DMSO, 0.4 mL) and stirring for 1 hour at room temperature. For deposition of perovskite films, the $CH_3NH_3PbI_3$ precursor solution (50 µL) was first dropped onto a TiO_2/SbI_3 coated FTO substrate. The substrate was spun at 4000 rpm for 25 s, and at 4000 rpm for 10 seconds, during which, 500 µL anhydrous ethyl acetate was quickly dropped onto the center of the substrate. The obtained films were then dried at 65 °C for 1 min and 100 °C for 10 min. The hole-transporting layer was deposited by spin coating 20 µL of 2,2′,7,7′-tetrakis(N,N-di-p-methoxyphenylamine)-9,9-spirobifluorene (spiro-OMeTAD) solution on top of $CH_3NH_3PbI_3$. The spiro-OMeTAD solution was prepared by dissolving 72.3 mg of spiro-OMeTAD in 1 mL of chlorobenzene, to which 28.8 µL of 4-tert-butyl pyridine (4-TBP) and 17.5 µL of lithium bis(trifluoromethanesulfonyl)imide (Li-TFSI) solution (520 mg LI-TSFI in 1 mL acetonitrile) were added. Finally, an 80-nm-thick Au was thermally evaporated on the spiro-OMeTAD-coated film as the cathode. The whole process was carried out in the air environment without using a glove box. Note the following points: (a), the substrate was treated with oxygen plasma before making the perovskite; (b), before spin coating, perovskite precursor solution and spiro-OMeTAD solution were filtered by 0.45 µm PVDF syringe filter; (c), after spin-coating spiro-OMeTAD, the samples were kept in a desiccator overnight and Au electrode was evaporated the next day.

Film characterization. A field-emission scanning electron microscope (FE-SEM, Jeol JSM 6700F) and a Bruker Innova atomic force microscopy (AFM) (JSPM-5200) were used to investigate the surface morphology of the samples. UV-Vis spectra were obtained using a Shimadzu UV-2550 spectrophotometer. The photoelectron yield spectroscopy (PYS) was used to measure the valence-band maximum (VBM). X-ray diffraction (XRD) experiments were conducted by a Rigaku SmartLab X-ray diffractometer with Cu Kα radiation (λ=1.5418 Å), 45 kV and 200 mA at room temperature. The samples were scanned from 10° to 80° with a step-size of 0.01°.

Device characterization. Photocurrent and voltage were measured with a solar simulator (KHP-1, Bunko-Keiki, Japan) equipped with a xenon lamp (XLS-150A) and a Keithley 2400 source meter. The intensity of light irradiation was calibrated with a standard amorphous Si photodetector (BS-520 S/N 007, Bunko-Keiki, Japan), and adjusted to simulate the 1 SUN (100 mW·cm^{-2}) AM1.5G illumination. The voltage scan rate was 10 mV·s^{-1}. The devices were measured after stored for one day in a moisture-free desiccator. These samples were covered with a black metal mask (0.1 cm^2) to define the active area and reduce the influence of the scattered light. The electrochemical impedance spectrum (EIS) analysis was performed using an electrochemical measurement system (12528WB, Solartron Metrology) in the dark conditions with the frequency ranging from 10^5 to 10^{-1} Hz at an applied bias of 0.4, 0.6 and 0.8 V.

Results and discussion
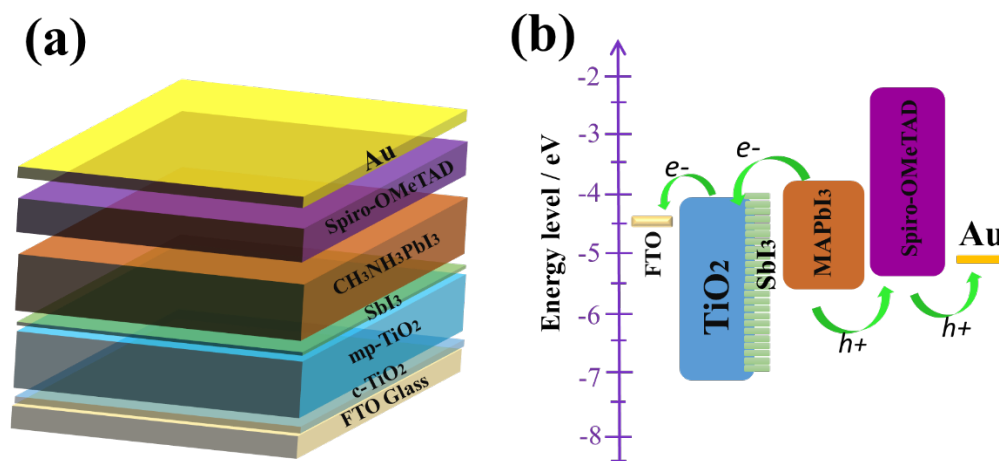
Fig. 1. The TiO$_2$/SbI$_3$/MAPbI$_3$/spiro-OMeTAD/Au solar cell: (a) the device structure, and (b) the energy band diagram.

The architecture of the prepared TiO$_2$/SbI$_3$-based perovskite solar cell, as illustrated in Fig. 1a, is FTO/c-TiO$_2$/m-TiO$_2$/SbI$_3$/MAPbI$_3$/spiro-OMeTAD/Au. The thin passivation layer, SbI$_3$, was introduced onto the TiO$_2$ surface by immersing TiO$_2$ film into SbI$_3$/DMF solution. It is expected that the SbI$_3$ thin layer can effectively passivate TiO$_2$ to reduce surface defects, and reduce electron-hole recombination which takes place at TiO$_2$ surface. The light absorption and valence-band maximum of TiO$_2$ and TiO$_2$/SbI$_3$ were measured by using a UV-vis spectrophotometer and photoelectron yield spectroscopy, as shown in Fig. S3. It is evident from the UV-Vis result that the surface passivation by SbI$_3$ does not affect the absorption of the TiO$_2$. The band gap, Eg determined from the UV-Vis spectra also showed no change before and after SbI$_3$ passivation suggesting that the surface of TiO$_2$ is passivated by a monolayer SbI$_3$ (3.20 eV, see inset figure in Fig. S3a). However, from the PYS measurement, passivating the TiO$_2$ surface with SbI$_3$ reduces the VBM from -7.45 eV to -7.13 eV (Fig. S3b). The reason for the lower VBM in the case of SbI$_3$ passivation is due to the lower VBM and Eg in the case of Sb$_2$O$_3$ and SbI$_3$. [28-29] The working mechanism of PYS is based on the photoelectric effect and thus the measurement is very sensitive to the surface condition of the sample, therefore passivation with a monolayer resulted in different values as shown in Fig S3b. Fig. 1b shows the schematic energy level diagram of the device. In this configuration, based on the matching energy level of each layer in the device components, the electrons and holes originated from MAPbI$_3$ perovskite can be easily be injected into TiO$_2$ and spiro-OMeTAD, respectively.
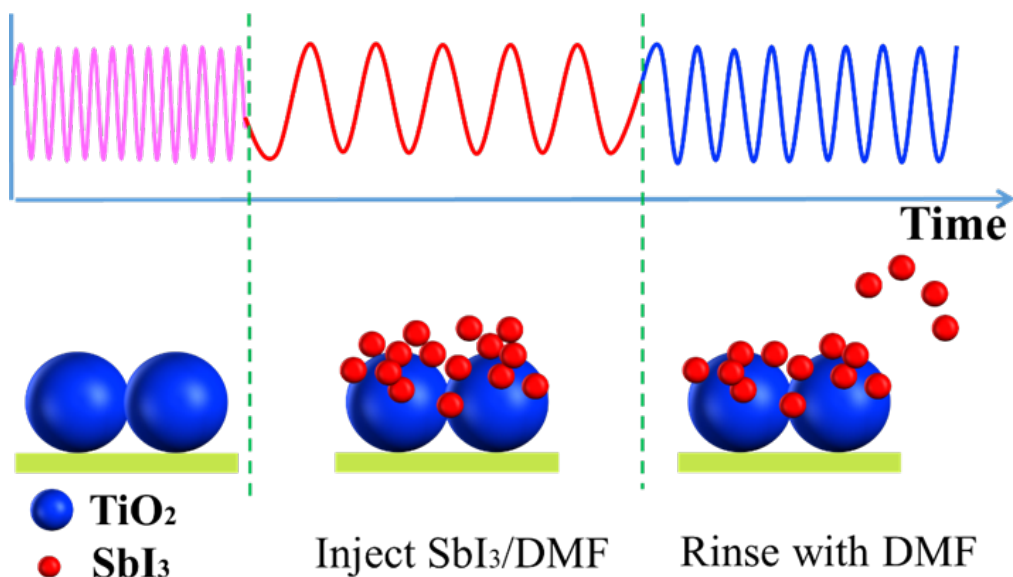
Fig. 2 Schematic diagram of adsorption and rinsing process of SbI_3 on TiO_2 surfaces and the change in the vibrational frequency.
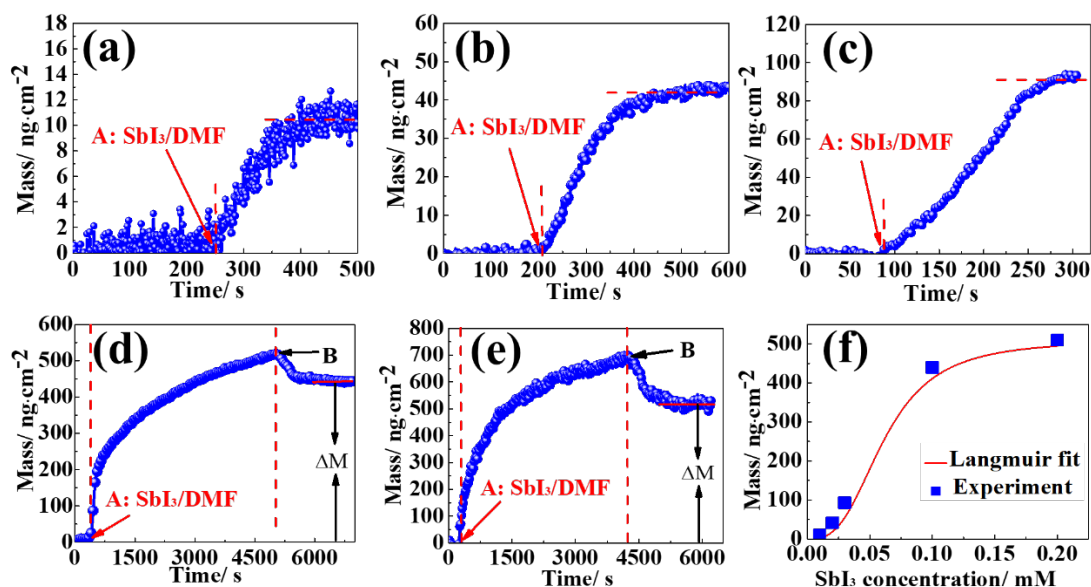
Fig. 3 Relationship between SbI_3 adsorption density on TiO_2 and the adsorption time. Mass was calculated via the Sauerbrey equation from frequency data. The concentration of SbI_3/DMF is (a) 0.01 mM, (b) 0.02 mM, (c) 0.03 mM, (d) 0.1 mM and (e) 0.2 mM. (f) Absorption mass at different concentrations. The solid red line indicates a nonlinear least-square fit to the Langmuir model.

To investigate the kinetics of SbI_3 adsorption to TiO_2, we utilized a quartz crystal microbalance (QCM) measurement system, which monitors the SbI_3 adsorption on the TiO_2

5

surface. When the SbI$_3$/DMF solution flows over the surface of TiO$_2$-QCM-sensor, the SbI$_3$ molecule binds to -OH on the surface of TiO$_2$, resulting in a decrease in the vibration frequency of the TiO$_2$-QCM-sensor. As shown in Fig 2, SbI$_3$ is firstly adsorbed on the surface of TiO$_2$. After that, the surface is washed with solvent to remove the additional SbI$_3$. Fig. 3 (a-e) shows the adsorbed mass on a TiO$_2$ surface in SbI$_3$/DMF solution with a concentration from 0.01 to 0.2 mM. The SbI$_3$ solution was introduced to the TiO$_2$ sensor surface at point A in the figure. With the increase in adsorption time, the mass is getting higher, but the rate of mass increase is becoming slower. The substrates were then rinsed with pure DMF solution at point B in Fig. 3 (d,e) to remove weakly bound SbI$_3$ molecules from the TiO$_2$ surface. Due to the presence of -OH groups on the TiO$_2$ surface[30-31], SbI$_3$ can react with -OH to form Ti-O-Sb bonds.
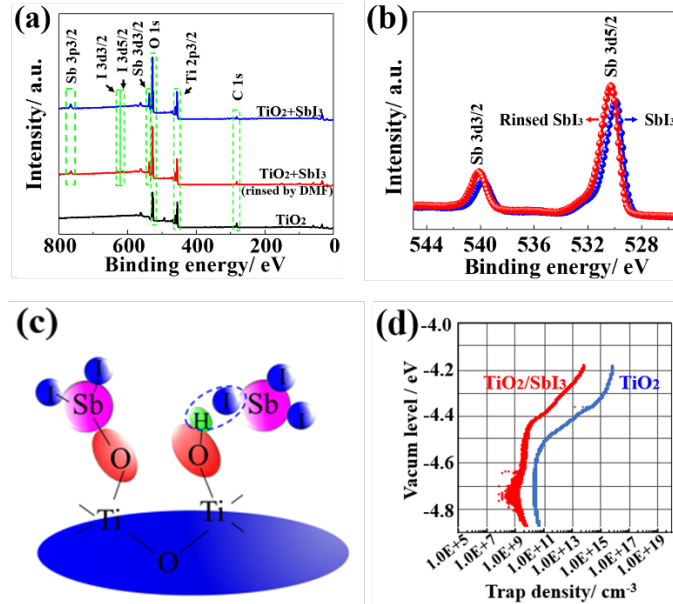
Fig. 4 (a) XPS wide scan of TiO$_2$ film and SbI$_3$-adsorbed TiO$_2$ film, (b) High-resolution XPS spectra of Sb adsorbed on TiO$_2$ surface (spectra of Sb 3d5/2 and Sb 3d3/2). (c) Schematic diagram portraying the reaction of SbI$_3$ with the -OH of TiO$_2$. (d) Trap distribution of porous TiO$_2$ and TiO$_2$/SbI$_3$.

Fig. 4 (a) shows the XPS full spectrum of bare TiO$_2$ (black curve) and SbI$_3$-adsorbed TiO$_2$ (blue and red curves). In the sample after rinsing with DMF, peaks corresponding to Sb elements still exist, indicating that Sb element was successfully incorporated in the TiO$_2$ surface. Peaks at 539.4 and 766.4 eV are assigned to Sb 3d3/2 and Sb 3p3/2, respectively. The peaks at 616.17 and 628.19 eV can be assigned to I 3d5/2 and I 3d3/2, respectively. The XPS spectra of Sb 3d of TiO$_2$/SbI$_3$ samples is shown in Fig. 4 (b). Before rinsing with DMF, the peak of Sb 3d5/2 and Sb 3d3/2 were observed at 529.18 and 539.77 eV. After rinsing, the Sb 3d peak pairs shift to higher binding energy location. This suggests that Ti-O-Sb linkages are formed at the TiO$_2$ surface. The schematic diagram showing the reaction of SbI$_3$ with TiO$_2$ is shown in Fig. 4c. It is understood from the XPS result that the hydroxyl (-OH) on TiO$_2$ surface react with Sb-I to form Ti-O-Sb. The reaction mechanism is shown in Formula (i). A similar observation with PbI$_2$ has been reported previously by Nakayashiki et al.[30, 32]

6

Ti-OH + SbI$_3$ → Ti-O-Sb + HI   (i)

The positively charged Sb is nucleophilically attacked by negatively charged O of Ti-O to form Ti-O-Sb bond and generate HI molecular. In order to further explore the influence of the passivation layer of SbI$_3$ on the surface of TiO$_2$, the surface electron trap distribution of the films was measured by using thermally stimulated current method (TSC). As shown in Fig. 4(d), the trap density of the bare TiO$_2$ at a vacuum level of -4.2 eV is 10^{16}/cm^3, while that of the TiO$_2$/SbI$_3$ film was significantly reduced at -4.2 eV (10^{14}/cm^3). It has been reported that surface trap acts as recombination center[32]. The low trap density upon passivation with SbI$_3$ is expected to reduce electron-hole recombination and hence helped to improve the performance of the solar cells.[33]
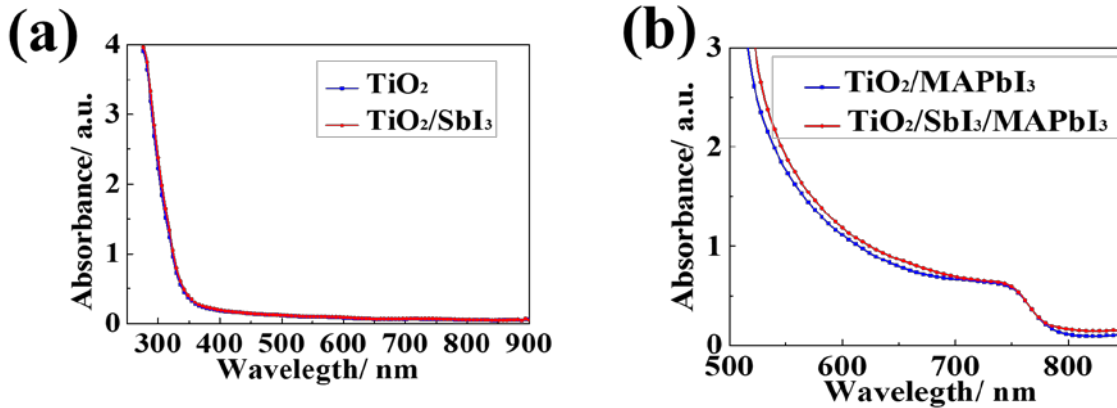
Fig. 5. UV-visible absorption spectra of (a) TiO$_2$, TiO$_2$/SbI$_3$ film, and (b) perovskite film on TiO$_2$ and TiO$_2$/SbI$_3$ substrates.

In order to confirm the change of the surface properties of the films before and after passivation, we measured the contact angle of water on the films (see the supporting information Fig. S4). After passivation, the contact angle increased significantly (from 23.6^o to 40.5^o), indicating that the -OH on the surface of TiO$_2$ decreased. This supports the results of QCM, XPS, and TSC data shown in Fig. 3 and Fig. 4. On device fabrication, the TiO$_2$ surface is treated with plasma. Hydrophilicity of the thin film after plasma treatment is enhanced, but the contact angle of TiO$_2$/SbI$_3$ (6.4^o) is still larger than bare TiO$_2$ (2.6^o) (see Fig. S4c-d). The UV-vis absorption measurement of MAPbI$_3$ perovskite film prepared on TiO$_2$ and TiO$_2$/SbI$_3$ substrates were carried out to investigate the effect of the SbI$_3$ passivation layer on the light absorption of the perovskite films, as shown in Fig. 5a and 5b. The introduction of SbI$_3$ has little effect on the absorption of the TiO$_2$ film (See Fig. 5a). However, the absorption from 500 nm to 800 nm of the perovskite film was enhanced on the TiO$_2$/SbI$_3$ substrates. Fig. 6 (a) shows top-view SEM images of the MAPbI$_3$ film deposited on mp-TiO$_2$. It can be seen that there are some pin-holes on the perovskite film and is clearly visible at high magnification in Fig. 6 (b). While, in Fig. 6 (d) the perovskite films deposited on the TiO$_2$ passivated by SbI$_3$ were significantly improved, and the perovskite crystals were arranged more densely without pin-holes, at high magnification (Fig. 6 e). The TiO$_2$/SbI$_3$/MAPbI$_3$ film in Fig. 6f was smoother and denser, compared with TiO$_2$/MAPbI$_3$ film (Fig. 5 c). Corresponding 3D AFM images are shown in Fig. S5. In addition, the X-ray diffraction (XRD) spectra in Fig. S6 show that there is no significant crystallographic

difference of the perovskite layer between passivation and non-passivation cases; however, the full width at half maximum (FWHM) of perovskite is smaller for $TiO_2/SbI_3/MAPbI_3$ indicating SbI_3 passivation can increase the crystallinity of $MAPbI_3$.
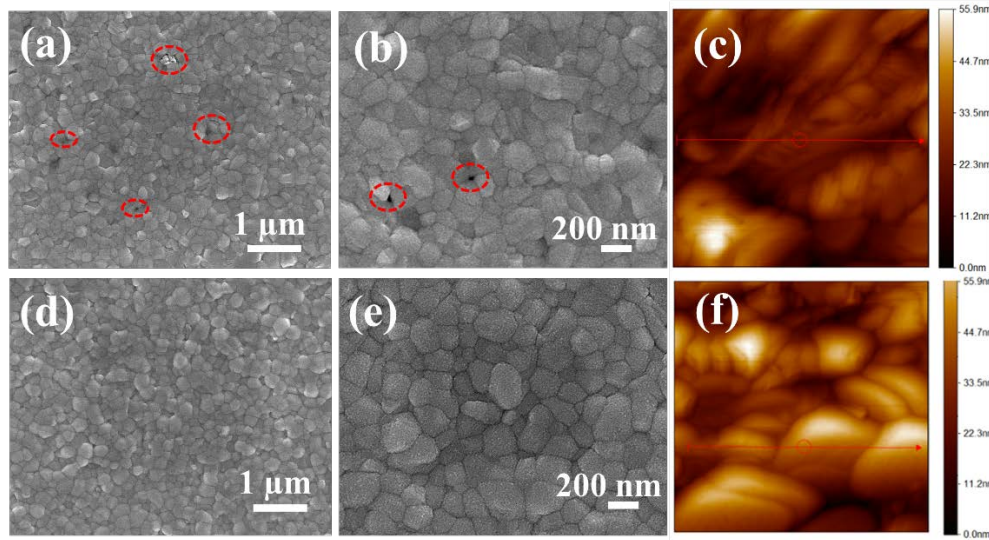
Fig. 6. Top-view of SEM (a, b, d, e) and 2D AFM (c, f) images of $MAPbI_3$ perovskite film deposited on (a, b, c) FTO/TiO_2 and (d, e, f) FTO/TiO_2/SbI_3.
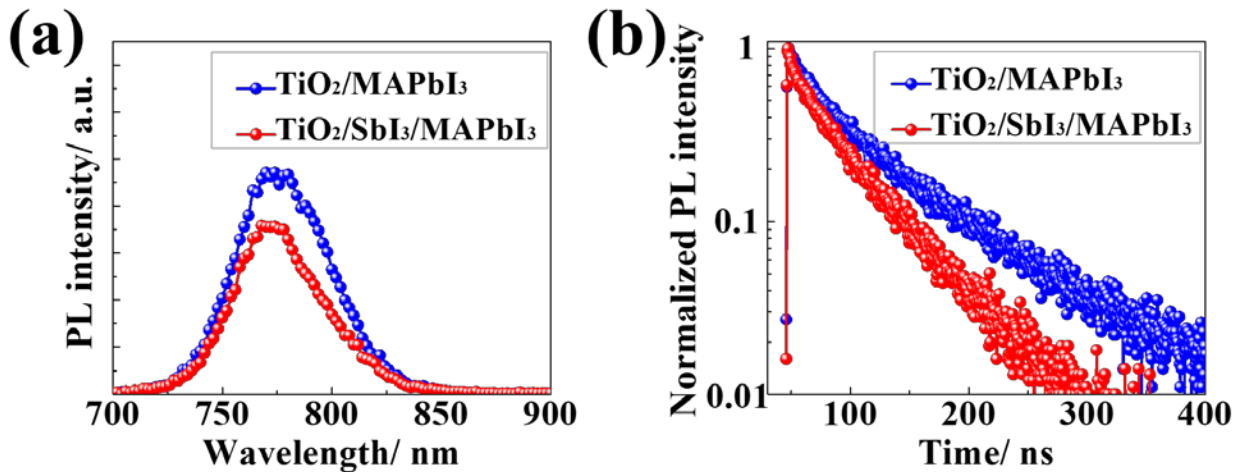
Fig. 7. (a) Steady-state PL spectra and (b) TRPL spectroscopy for perovskite films deposited on TiO_2 and TiO_2/SbI_3 substrates.

In order to better ascertain the effect of the SbI_3 passivation layer on electron transport, the charge dynamics of the perovskite film deposited on TiO_2 and TiO_2/SbI_3 were carefully examined by using PL spectroscopy. The steady-state PL and TRPL spectra as shown in Fig. 7. The PL quenching effect is an evidence of carrier charge separation at the interface. F ig.7 a portrays the PL quenching on perovskite film deposited on TiO_2/SbI_3 compared to that on bare

TiO$_2$, showing a faster electron transport after SbI$_3$ passivation. More interestingly, the perovskite film deposited on TiO$_2$/SbI$_3$ showed a slight blue-shifted PL peak from 774 nm to 772 nm compared with the non-passivation sample, which implies the SbI$_3$ passivation layer can effectively inhibit charge recombination.[34] The TRPL spectroscopy in Fig.7 b shows a significant reduction in decay time after passivation, again consistent with effective electron transfer to the SbI$_3$ modified TiO$_2$.
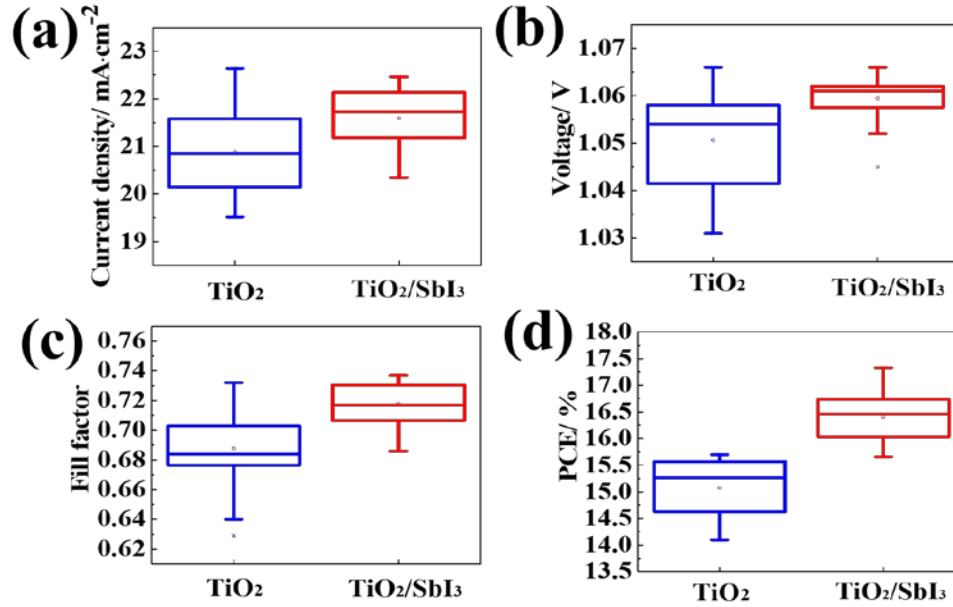
Fig. 8 Box charts of 20 independent solar cells in each group (a) J_{SC}, (b) V_{OC}, (c) FF and (d) PCE for perovskite solar cells based on TiO$_2$ and TiO$_2$/SbI$_3$.

Fig. 8 (a-d) are the box charts of detailed photovoltaic performance. After the passivation of the TiO$_2$ electron transport layer with SbI$_3$, the solar cell performance was significantly improved. As mentioned above, after passivation, the concentration of trap on the TiO$_2$ surface decreased. This decreases the chance of electrons and holes recombining on the TiO$_2$ surface, resulting in a higher open circuit voltage and fill factor. The photovoltaic parameters are shown in Tab. S1 and S2.
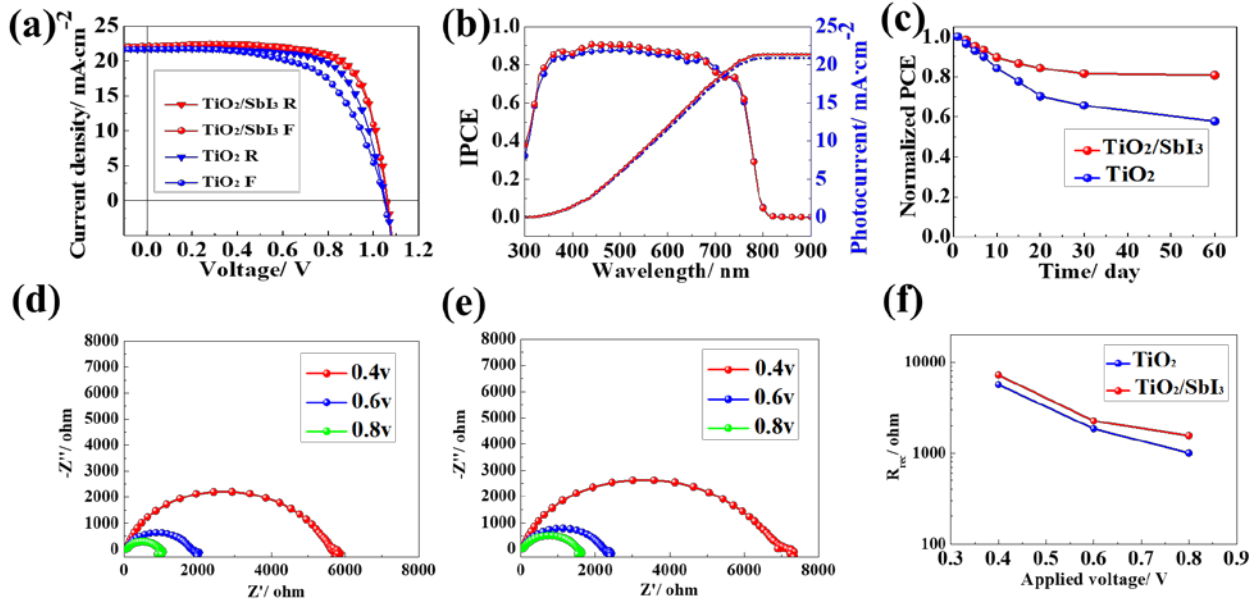
Fig. 9 (a) J-V curves and (b) IPCE spectra of the champion devices based on TiO_2 and TiO_2/SbI_3. (c) Stability test for TiO_2 and TiO_2/SbI_3 based perovskite solar cells. The devices were stored in a ~50% humidity air environment. Nyquist plots of devices based on (d) TiO_2 and (e) TiO_2/SbI_3 measured in dark condition with different forward applied bias (0.4, 0.6 and 0.8v). (f) Carrier recombination resistance extracted from EIS measurements at varied bias potentials.

J-V and IPCE characteristics of the solar cells with the highest PCE based on TiO_2 and TiO_2/SbI_3 are shown in Fig. 9 (a, b). TiO_2 based solar cell showed a large hysteresis, while the solar cell based on TiO_2/SbI_3 showed almost no hysteresis. As previously reported, such photocurrent hysteresis is also typically observed in many kinds of electronic devices, particularly defect-rich, organic-based electronic devices, which contain a non-negligible amount of charge traps [34-36]. In this work, after passivated with SbI_3, trap on TiO_2 surface obviously decrease, therefore, the hysteresis is effectively reduced. A high PCE of 17.33%, with J_{SC}, V_{OC}, and FF, of 1.06 V, 22.16 mA·cm^{-2}, and 0.74 respectively, were obtained under standard illumination conditions (AM 1.5G, 100 mW·cm^{-2}). Clearly, the application of a SbI_3 passivation layer increased the PCE from 15.82% (J_{SC}=21.65 mA·cm^{-2}, V_{OC}= 1.05 V and FF= 0.70) to 17.33%, which comes mainly from the enhanced J_{SC} and FF. To investigate the effect of SbI_3 passivation on the device stability, we have also measured the maximal steady-state photocurrent output of the two representative devices by applying a constant bias voltage (0.83 V for the TiO_2-based device, 0.87 V for the TiO_2/SbI_3-based device) taken from the maximum power points (MPP) in the J-V measurements. Fig S7 (a, b) show that the steady-state efficiency of the cells based on TiO_2 and TiO_2/SbI_3 are stabilized at 16.6% and 15.2%, respectively. In all, SbI_3 plays a very positive passivation effect on the electronic transport layer, resulting in an enhanced efficiency. The long-term stability of PSCs is closely related to the front ESL/perovskite interfacial charge accumulation during operation [7, 37-38]. We examined the long-term stability of PSCs based on TiO_2/SbI_3 and TiO_2. The unencapsulated solar cells for long-term stability test were done in air condition with about 50% humidity at room temperature for two months. Fig. 9 (c) presents the PCE change of both devices as a function of aging time. The devices based on TiO_2/SbI_3 showed enhanced stability,

maintained 81% of the initial PCE after storage in air condition for 60 days, whereas those based on TiO$_2$ retained 58% of their initial efficiency.

To further investigate the interfacial charge transport process in the device, EIS measurement was performed for TiO$_2$ and TiO$_2$/SbI$_3$ based perovskite solar under a dark condition at different applied bias. The Nyquist plot in Fig. 9 (d) and (e) shows the typical semicircles. Based on the previous report, the semicircle could be related to the overall charge transport in the devices [31, 39]. From Fig. 9 (f), at the same bias compare to the TiO$_2$-based device, the TiO$_2$/SbI$_3$-based device shows a higher charge recombination resistance. Theoretically, a large recombination resistance favors delayed carrier recombination and helps to increase the FF, which is consistent with the box chart in Fig. 7 (c)[40-41].

Conclusions

In summary, we demonstrated that the interface between the electron transporting layer and perovskite is important for device performance of perovskite solar cells. The thin SbI$_3$ passivation layer was prepared by a simple immersion method which can passivate the TiO$_2$ surface and thus effectively reduced the TiO$_2$ electronic trap states and enabled faster electron transport. QCM monitors of the adsorption of SbI$_2$ on TiO$_2$ surface, XPS and TSC result effectively proved that the surface trap concentration of TiO$_2$ after passivation was reduced. The solar cell efficiency with the SbI$_3$-passivated mesoporous TiO$_2$ electrodes was enhanced from 15.82% (15.04% in average) to over 17.33% (16.41% on average). Even after 60 days, the device still maintained more than 80% of the initial efficiency at air without encapsulation.

Acknowledgments

Supporting Information.

Additional data and results (Thickness, PYS, Contact angle, AFM images, XRD, MPP, photovoltaic parameters of perovskite solar cells) (PDF)

Corresponding Author

* Email: hayase@life.kyutech.ac.jp.

Notes

The authors declare no competing financial interest.

References

(1) Correa-Baena, J.-P.; Tress, W.; Domanski, K.; Anaraki, E. H.; Turren-Cruz, S.-H.; Roose, B.; Boix, P. P.; Grätzel, M.; Saliba, M.; Abate, A. Identifying and Suppressing Interfacial Recombination to Achieve

High Open-circuit Voltage in Perovskite Solar Cells. *Energy & Environmental Science* **2017,** *10*, 1207-1212.

(2) Fang, H.-H.; Adjokatse, S.; Shao, S.; Even, J.; Loi, M. A. Long-lived Hot-carrier Light Emission and Large Blue Shift in Formamidinium Tin Triiodide Perovskites. *Nature communications* **2018,** *9*, 243.

(3) Montcada, N. F.; Méndez, M.; Cho, K. T.; Nazeeruddin, M. K.; Palomares, E. Photo-induced Dynamic Processes in Perovskite Solar Cells: The Influence of Perovskite Composition in the Charge Extraction and the Carrier Recombination. *Nanoscale* **2018,** *10*, 6155-6158.

(4) Domanski, K.; Alharbi, E. A.; Hagfeldt, A.; Grätzel, M.; Tress, W. Systematic Investigation of the Impact of Operation Conditions on the Degradation Behaviour of Perovskite Solar Cells. *Nature Energy* **2018**, 1.

(5) Kojima, A.; Teshima, K.; Shirai, Y.; Miyasaka, T. Organometal Halide Perovskites as Visible-light Sensitizers for Photovoltaic Cells. *J. Am. Chem. Soc.* **2009,** *131*, 6050-6051.

(6) Yang, W. S.; Park, B.-W.; Jung, E. H.; Jeon, N. J.; Kim, Y. C.; Lee, D. U.; Shin, S. S.; Seo, J.; Kim, E. K.; Noh, J. H. Iodide Management in Formamidinium-Lead-Halide–Based Perovskite Layers for Efficient Solar Cells. *Science* **2017,** *356*, 1376-1379.

(7) Tan, H.; Jain, A.; Voznyy, O.; Lan, X.; de Arquer, F. P. G.; Fan, J. Z.; Quintero-Bermudez, R.; Yuan, M.; Zhang, B.; Zhao, Y. Efficient and Stable Solution-processed Planar Perovskite Solar Cells via Contact Passivation. *Science* **2017,** *355*, 722-726.

(8) Shin, S. S.; Yeom, E. J.; Yang, W. S.; Hur, S.; Kim, M. G.; Im, J.; Seo, J.; Noh, J. H.; Seok, S. I. Colloidally Prepared La-doped $BaSnO_3$ Electrodes for Efficient, Photostable Perovskite Solar Cells. *Science* **2017,** *356*, 167-171.

(9) Correa-Baena, J.-P.; Nienhaus, L.; Kurchin, R. C.; Shin, S. S.; Wieghold, S.; Hartono, N. T. P.; Layurova, M.; Klein, N. D.; Poindexter, J. R.; Polizzotti, A. A-site Cation in Inorganic $A_3Sb_2I_9$ Perovskite Influences Structural Dimensionality, Exciton Binding Energy, and Solar Cell Performance. *Chem. Mater.* **2018**.

(10) Yang, F.; Kapil, G.; Zhang, P.; Hu, Z.; Kamarudin, M. A.; Ma, T.; Hayase, S. Dependence of Acetate-Based Antisolvents for High Humidity Fabrication of $CH_3NH_3PbI_3$ Perovskite Devices in Ambient Atmosphere. *ACS applied materials & interfaces* **2018**.

(11) Fu, N.; Huang, C.; Liu, Y.; Li, X.; Lu, W.; Zhou, L.; Peng, F.; Liu, Y.; Huang, H. Organic-free Anatase TiO_2 Paste for Efficient Plastic Dye-sensitized Solar Cells and Low Temperature Processed Perovskite Solar Cells. *ACS applied materials & interfaces* **2015,** *7*, 19431-19438.

(12) Sidhik, S.; Cerdan-Pasaran, A.; Esparza, D.; Lopez-Luke, T.; Carriles, R.; De La Rosa, E. Improving the Optoelectronic Properties of Mesoporous TiO_2 by Cobalt Doping for High-performance Hysteresis-free Perovskite Solar Cells. *ACS applied materials & interfaces* **2018**.

(13) Giordano, F.; Abate, A.; Baena, J. P. C.; Saliba, M.; Matsui, T.; Im, S. H.; Zakeeruddin, S. M.; Nazeeruddin, M. K.; Hagfeldt, A.; Graetzel, M. Enhanced Electronic Properties in Mesoporous TiO_2 via Lithium Doping for High-efficiency Perovskite Solar Cells. *Nature communications* **2016,** *7*, 10379.

(14) Matsui, T.; Seo, J. Y.; Saliba, M.; Zakeeruddin, S. M.; Grätzel, M. Room-temperature Formation of Highly Crystalline Multication Perovskites for Efficient, Low-cost Solar Cells. *Adv. Mater.* **2017,** *29*.

(15) Liu, D.; Li, S.; Zhang, P.; Wang, Y.; Zhang, R.; Sarvari, H.; Wang, F.; Wu, J.; Wang, Z.; Chen, Z. D. Efficient Planar Heterojunction Perovskite Solar Cells with Li-doped Compact TiO_2 Layer. *Nano Energy* **2017,** *31*, 462-468.

(16) Zhang, H.; Shi, J.; Xu, X.; Zhu, L.; Luo, Y.; Li, D.; Meng, Q. Mg-doped TiO_2 Boosts the Efficiency of Planar Perovskite Solar Cells to Exceed 19%. *Journal of Materials Chemistry A* **2016,** *4*, 15383-15389.

(17) Singh, T.; Öz, S.; Sasinska, A.; Frohnhoven, R.; Mathur, S.; Miyasaka, T. Sulfate-assisted Interfacial Engineering for High Yield and Efficiency of Triple Cation Perovskite Solar Cells with Alkali-doped TiO_2 Electron-transporting Layers. *Adv. Funct. Mater.* **2018**, 1706287.

(18) Xu, Z.; Yin, X.; Guo, Y.; Pu, Y.; He, M. Ru-doping in TiO_2 Electron Transport Layers of Planar Heterojunction Perovskite Solar Cells for Enhanced Performance. *Journal of Materials Chemistry C* **2018**.

(19) Kim, D. H.; Han, G. S.; Seong, W. M.; Lee, J. W.; Kim, B. J.; Park, N. G.; Hong, K. S.; Lee, S.; Jung, H. S. Niobium Doping Effects on TiO_2 Mesoscopic Electron Transport Layer‐based Perovskite Solar Cells. *ChemSusChem* **2015**, *8*, 2392-2398.

(20) Zhou, H.; Chen, Q.; Li, G.; Luo, S.; Song, T.-b.; Duan, H.-S.; Hong, Z.; You, J.; Liu, Y.; Yang, Y. Interface Engineering of Highly Efficient Perovskite Solar Cells. *Science* **2014**, *345*, 542-546.

(21) Cai, Q.; Zhang, Y.; Liang, C.; Li, P.; Gu, H.; Liu, X.; Wang, J.; Shentu, Z.; Fan, J.; Shao, G. Enhancing Efficiency of Planar Structure Perovskite Solar Cells Using Sn-doped TiO_2 as Electron Transport Layer at Low Temperature. *Electrochim. Acta* **2018**, *261*, 227-235.

(22) Peng, J.; Wu, Y.; Ye, W.; Jacobs, D. A.; Shen, H.; Fu, X.; Wan, Y.; Wu, N.; Barugkin, C.; Nguyen, H. T. Interface Passivation Using Ultrathin Polymer–fullerene Films for High-efficiency Perovskite Solar Cells with Negligible Hysteresis. *Energy & Environmental Science* **2017**, *10*, 1792-1800.

(23) Pérez-del-Rey, D.; Boix, P. P.; Sessolo, M.; Hadipour, A.; Bolink, H. J. Interfacial Modification for High-efficiency Vapor-phase-deposited Perovskite Solar Cells Based on A Metal Oxide Buffer Layer. *The journal of physical chemistry letters* **2018**, *9*, 1041-1046.

(24) Tavakoli, M. M.; Giordano, F.; Zakeeruddin, S. M.; Grätzel, M. Mesoscopic Oxide Double Layer as Electron Specific Contact for Highly Efficient and Uv Stable Perovskite Photovoltaics. *Nano Lett.* **2018**.

(25) Seo, J. Y.; Uchida, R.; Kim, H. S.; Saygili, Y.; Luo, J.; Moore, C.; Kerrod, J.; Wagstaff, A.; Eklund, M.; McIntyre, R. Boosting the Efficiency of Perovskite Solar Cells with CsBr‐modified Mesoporous TiO_2 Beads as Electron‐ Selective Contact. *Adv. Funct. Mater.* **2018**.

(26) You, S.; Wang, H.; Bi, S.; Zhou, J.; Qin, L.; Qiu, X.; Zhao, Z.; Xu, Y.; Zhang, Y.; Shi, X. A Biopolymer Heparin Sodium Interlayer Anchoring TiO_2 and $MAPbI_3$ Enhances Trap Passivation and Device Stability in Perovskite Solar Cells. *Adv. Mater.* **2018**, 1706924.

(27) Im, J.-H.; Jang, I.-H.; Pellet, N.; Grätzel, M.; Park, N.-G. Growth of $CH_3NH_3PbI_3$ Cuboids with Ccontrolled Size for High-efficiency Perovskite Solar Cells. *Nature nanotechnology* **2014,** *9*, 927-932.

(28) He, G.-H.; Liang, C.-J.; Ou, Y.-D.; Liu, D.-N.; Fang, Y.-P.; Xu, Y.-H. Preparation of Novel Sb_2O_3/WO_3 Photocatalysts and Their Activities Under Visible Light Irradiation. *Mater. Res. Bull.* **2013,** *48*, 2244-2249.

(29) Liu, P.; Lu, F.; Wu, M.; Luo, X.; Cheng, Y.; Wang, X.-W.; Wang, W.; Wang, W.-H.; Liu, H.; Cho, K. Electronic Structures and Band Alignments of Monolayer Metal Trihalide Semiconductors MX_3. *Journal of Materials Chemistry C* **2017**, *5*, 9066-9071.

(30) Nakayashiki, S.; Daisuke, H.; Ogomi, Y.; Hayase, S. Interface Structure Between Titania and Perovskite Materials Observed by Quartz Crystal Microbalance System. *Journal of Photonics for Energy* **2015**, *5*, 057410.

(31) Zhu, X.; Yang, D.; Yang, R.; Yang, B.; Yang, Z.; Ren, X.; Zhang, J.; Niu, J.; Feng, J.; Liu, S. F. Superior Stability for Perovskite Solar Cells with 20% Efficiency Using Vacuum Co-evaporation. *Nanoscale* **2017**, *9*, 12316-12323.

(32) Zhang, F.; Song, J.; Hu, R.; Xiang, Y.; He, J.; Hao, Y.; Lian, J.; Zhang, B.; Zeng, P.; Qu, J. Interfacial Passivation of the P‐doped Hole‐transporting Layer Using General Insulating Polymers for High‐performance Inverted Perovskite Solar Cells. *Small* **2018**, 1704007.

(33) Ogomi, Y.; Morita, A.; Tsukamoto, S.; Saitho, T.; Shen, Q.; Toyoda, T.; Yoshino, K.; Pandey, S. S.; Ma, T.; Hayase, S. All-solid Perovskite Solar Cells with HOCO-R-NH_3+I–Anchor-Group Inserted Between Porous Titania and Perovskite. *The Journal of Physical Chemistry C* **2014**, *118*, 16651-16659.

(34) Shao, Y.; Xiao, Z.; Bi, C.; Yuan, Y.; Huang, J. Origin and Elimination of Photocurrent Hysteresis by Fullerene Passivation in $CH_3NH_3PbI_3$ Planar Heterojunction Solar Cells. *Nature communications* **2014,** *5*, 5784.

(35) Campos, A.; Riera-Galindo, S.; Puigdollers, J.; Mas-Torrent, M. Reduction of Charge Traps and Stability Enhancement in Solution-Processed Organic Field-effect Transistors Based on a Blended N-type Semiconductor. *ACS applied materials & interfaces* **2018**.

(36) Xiao, X.; Bao, C.; Fang, Y.; Dai, J.; Ecker, B. R.; Wang, C.; Lin, Y.; Tang, S.; Liu, Y.; Deng, Y. Argon Plasma Treatment to Tune Perovskite Surface Composition for High Efficiency Solar Cells and Fast Photodetectors. *Adv. Mater.* **2018**.

(37) Lee, Y. I.; Jeon, N. J.; Kim, B. J.; Shim, H.; Yang, T. Y.; Seok, S. I.; Seo, J.; Im, S. G. A Low-temperature Thin-film Encapsulation for Enhanced Stability of a Highly Efficient Perovskite Solar Cell. *Advanced Energy Materials* **2018,** *8*, 1701928.

(38) Halvani Anaraki, E.; Kermanpur, A.; Mayer, M. T.; Steier, L.; Ahmed, T.; Turren-Cruz, S.-H.; Seo, J.; Luo, J.; Zakeeruddin, S. M.; Tress, W. R. Low-temperature Nb-doped SnO_2 Electron-selective Contact Yields Over 20% Efficiency in Planar Perovskite Solar Cells. *ACS Energy Letters* **2018,** *3*, 773-778.

(39) Wei, H.; Xiao, J.; Yang, Y.; Lv, S.; Shi, J.; Xu, X.; Dong, J.; Luo, Y.; Li, D.; Meng, Q. Free-standing Flexible Carbon Electrode for Highly Efficient Hole-conductor-free Perovskite Solar Cells. *Carbon* **2015,** *93*, 861-868.

(40) Li, W.; Dong, H.; Guo, X.; Li, N.; Li, J.; Niu, G.; Wang, L. Graphene Oxide as Dual Functional Interface Modifier for Improving Wettability and Retarding Recombination in Hybrid Perovskite Solar Cells. *Journal of Materials Chemistry A* **2014,** *2*, 20105-20111.

(41) Stolterfoht, M.; Wolff, C. M.; Amir, Y.; Paulke, A.; Perdigón-Toro, L.; Caprioglio, P.; Neher, D. Approaching the Fill Factor Shockley–queisser Limit in Stable, Dopant-free Triple Cation Perovskite Solar Cells. *Energy & Environmental Science* **2017,** *10*, 1530-1539.

TOC

TiO₂
SbI₃

Inject SbI₃/DMF   Rinse with DMF
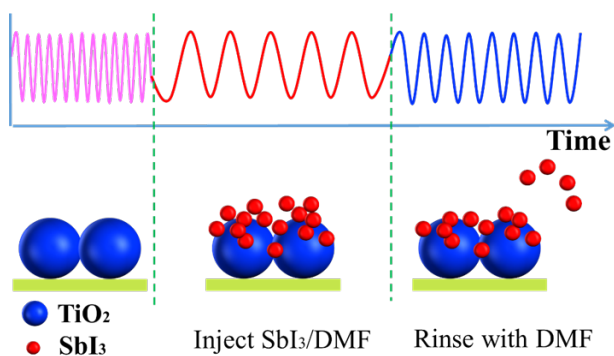
Supporting Information

Performance enhancement of mesoporous TiO$_2$-based perovskite solar cells by SbI$_3$ interfacial modification layer

Putao Zhang, Fu Yang, Muhammad Akmal Kamarudin, Chi Huey Ng, Gaurav Kapil, Tingli Ma,

Shuzi Hayase*

Graduate School of Life Science and Systems Engineering, Kyushu Institute of Technology, 2-4

Hibikino, Wakamatsu-ku, Kitakyushu, Fukuoka 808-0196, Japan

*Corresponding author: hayase@life.kyutech.ac.jp

Tel: +81-936956044, Fax: +81-936965000
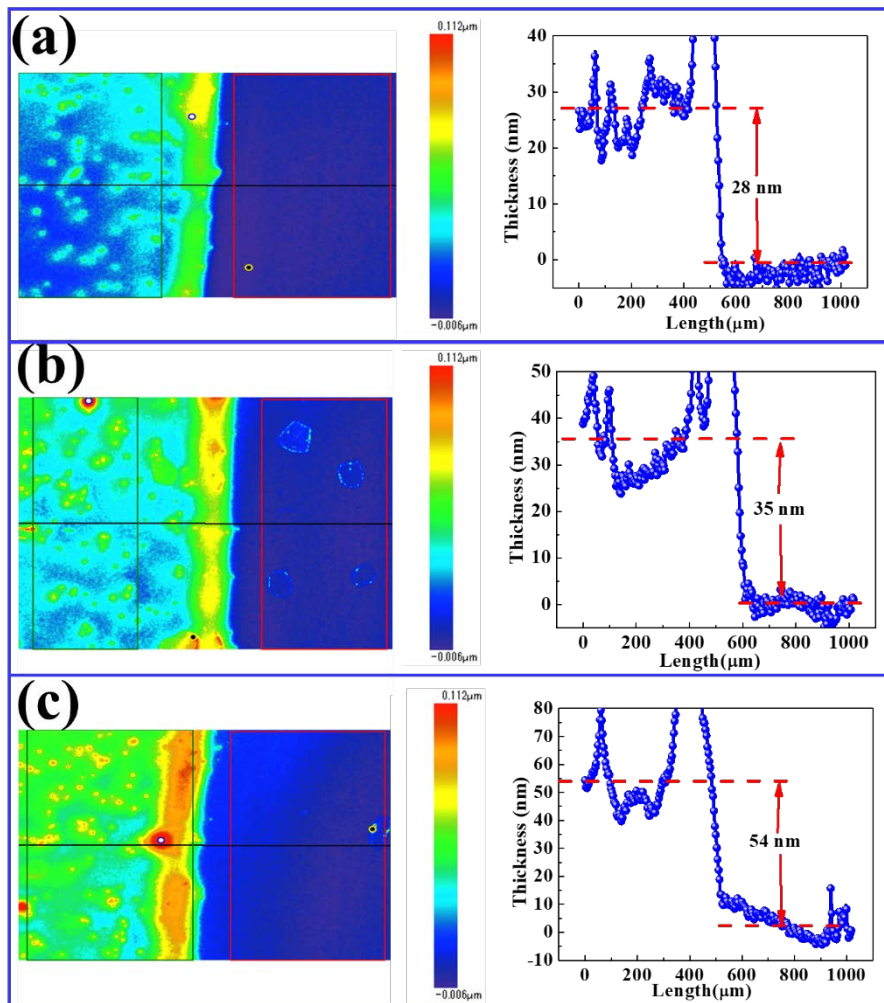
Fig. S1 Thickness of TiO₂ compact layer (c-TiO₂) on FTO glass. (a) 28 nm, (b) 35 nm, (c) 54 nm. The c-TiO₂ were prepared by spin-coating mothed, in detail 0.15 M titanium diisopropoxide bis (acetylacetonate) (75 wt% in isopropanol, Sigma-Aldrich) in 1-butanol (99.8%, Sigma-Aldrich) solution was spin-coated on an FTO substrate at 2000 rpm for 20 s, which was followed by heating on a hotplate at 125 °C for 5 min. Three samples were randomly selected with an average thickness of 39 nm ((28+35+54)/3=39 nm).
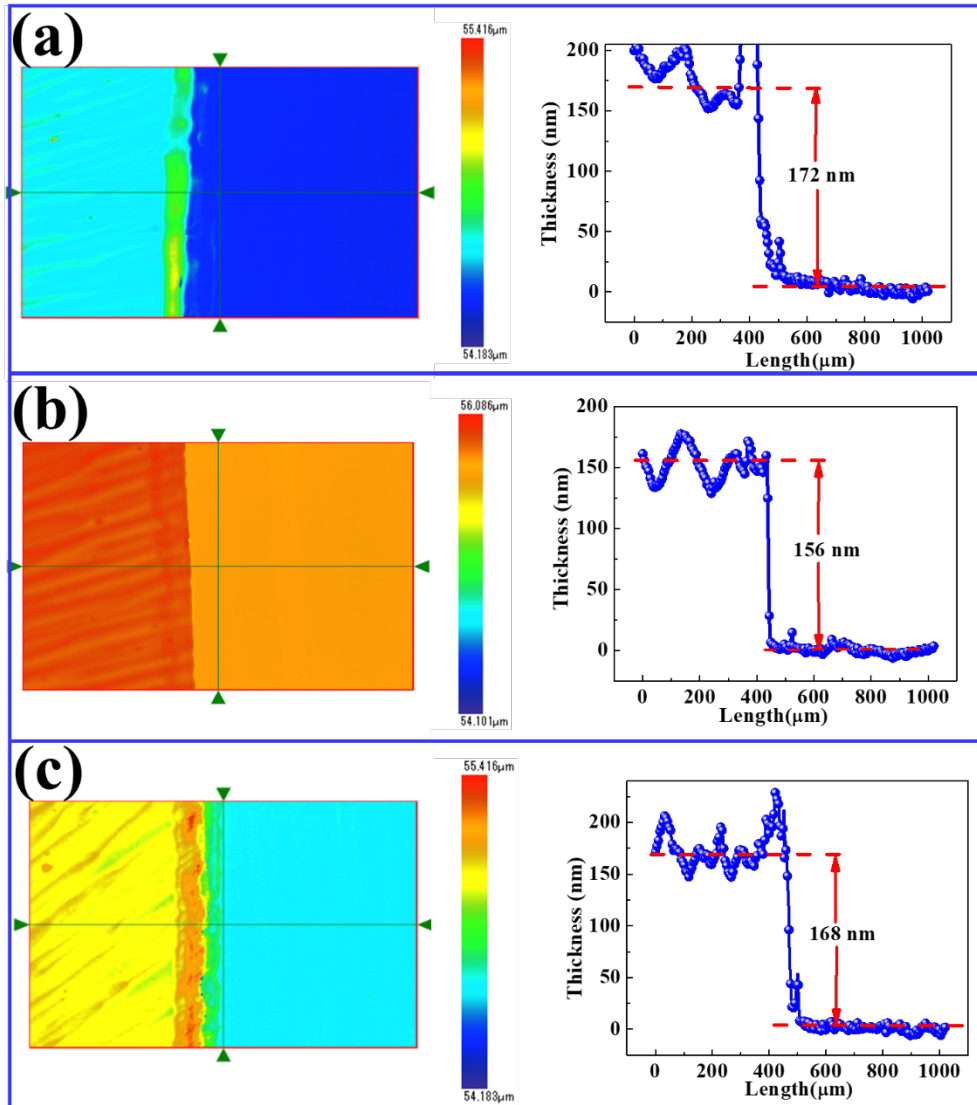
Fig. S2 Thickness of mesoporousTiO$_2$ layer (mp-TiO$_2$) on FTO/c-TiO$_2$. (a) 172 nm, (b) 156 nm, (c) 168 nm. In detail, dilute TiO$_2$ paste was spin-coated on the c-TiO$_2$ layer at 5000 rpm for 30 s, where the paste (Dyesol, 30 NR-D) was diluted in ethanol (TiO$_2$ paste/ethanol = 1/ 4, weight ratio). After drying on a hotplate at 125 °C for 5 min, the film was annealed at 500 °C for 1 h, providing an mp-TiO$_2$ with a thickness of about 165 nm. Three samples were randomly selected. ((172+156+168)/3=165 nm).
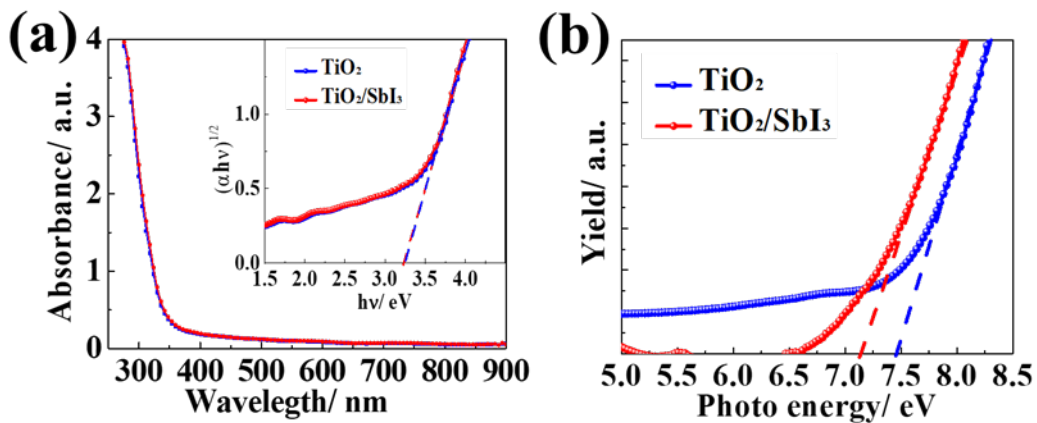
Fig. S3 (a) UV-visible absorption and (b) photoelectron yield (PY) spectra of the TiO$_2$ and TiO$_2$/SbI$_3$ films. Inset figure, the Tauc plot of band gap for TiO$_2$ and TiO$_2$/SbI$_3$ films.
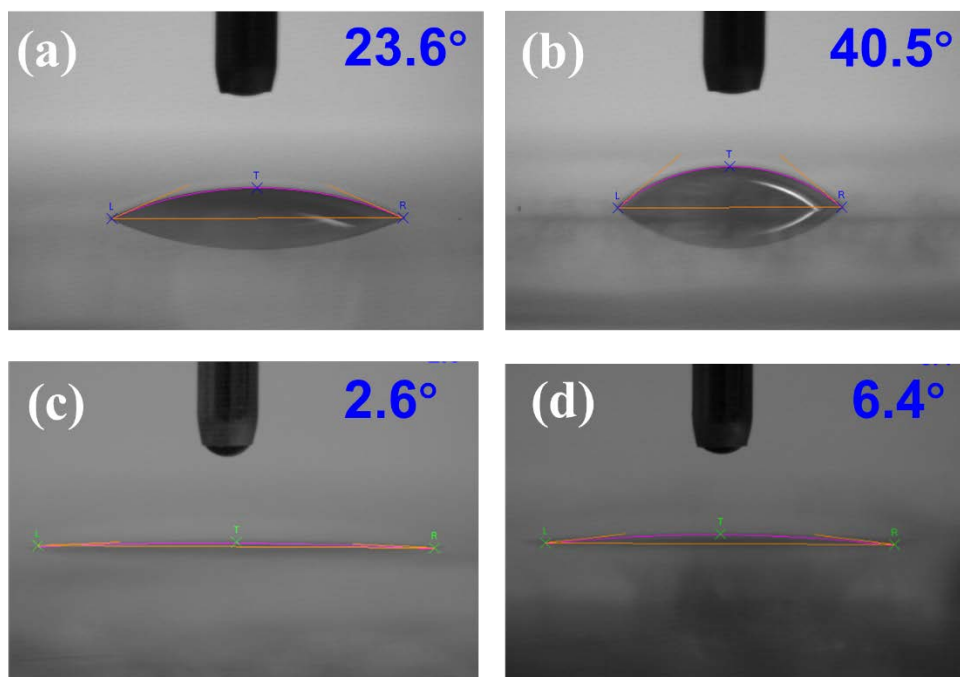
Fig. S4 Contact angle measurement for water on (a) TiO$_2$ and (b) TiO$_2$/SbI$_3$ films. After plasma treatment the contact angle for water on (c) TiO$_2$ and (d) TiO$_2$/SbI$_3$.
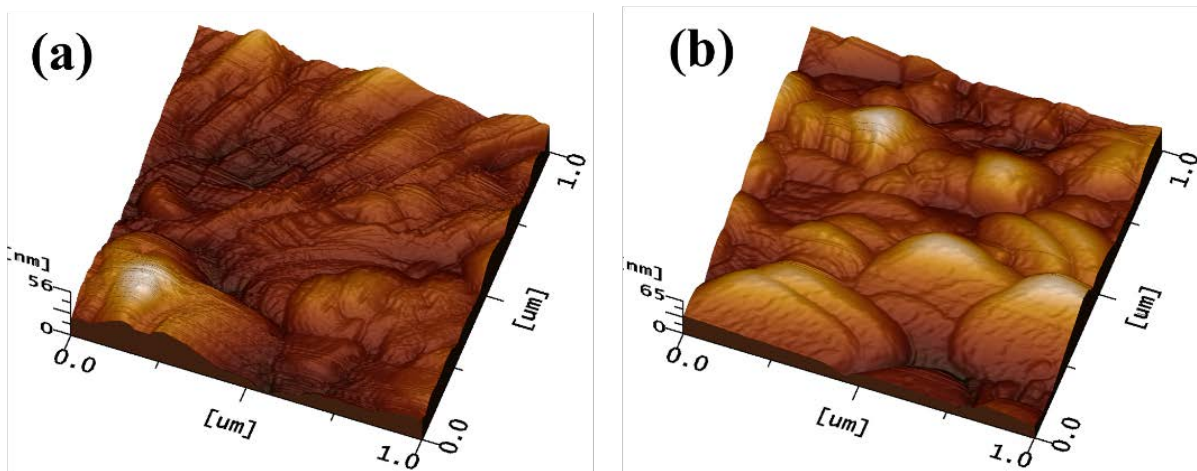
Fig. S5 3D AFM images of CH₃NH₃PbI₃ perovskite film deposited on (a) TiO_2 and (b) TiO_2/SbI_3 substrate.
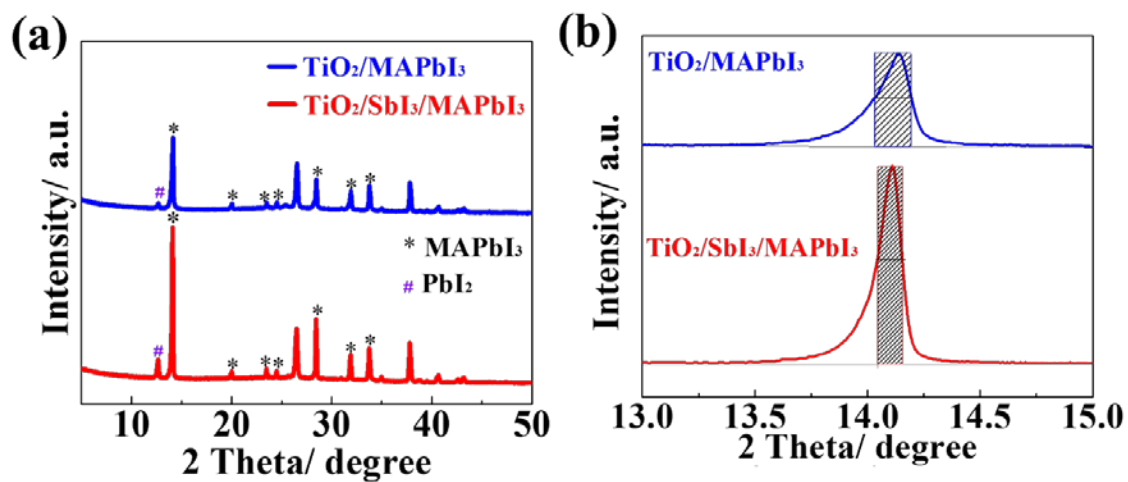
Fig. S6 (a) X-ray diffraction spectra of CH₃NH₃PbI₃ perovskite films deposited on TiO_2 (blue) and TiO_2/SbI_3 (red) substrate. (b) The full width at half maximum (FWHM) of the peak at 14.17°。
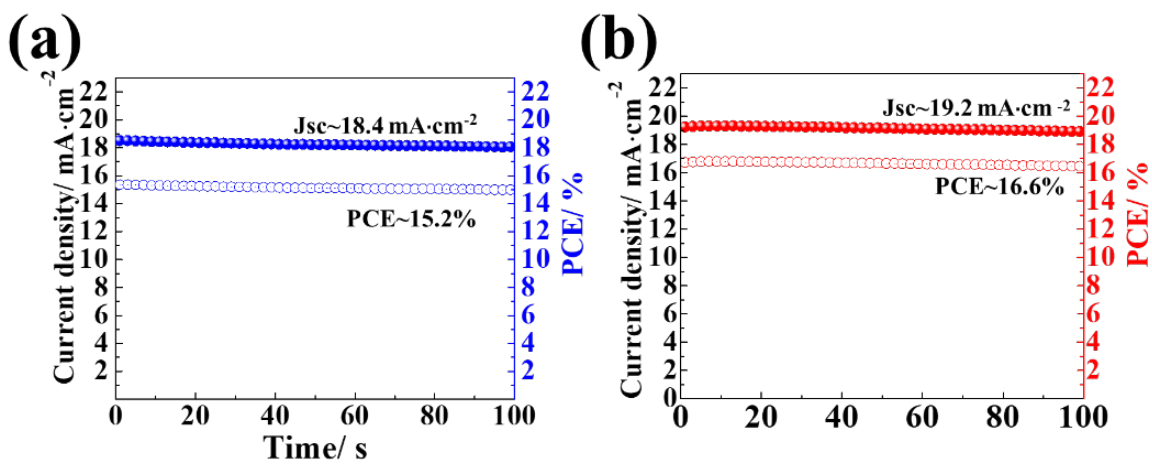
Fig. S7 Maximal steady-state photocurrent output of the solar cells, (a) at 0.83 V for the TiO$_2$-based device and (b) at 0.87 V for the TiO$_2$/SbI$_3$-based device, under constant 1 SUN illumination.

Tab. S1. Photovoltaic parameters for twenty perovskite solar cells based on the TiO_2/SbI_3 electronic transport layer. Average Jsc, Voc, FF and PCE were 21.592 mA·cm^{-2}, 1.059 V, 0.718 and 16.409%, respectively.

Device #	J_{sc} (mA·cm^{-2})	V_{oc} (V)	FF	PCE (%)
1	22.05	1.055	0.707	16.457
2	22.175	1.052	0.717	16.716
3	21.373	1.054	0.71	15.99
4	21.34	1.063	0.717	16.26
5	22.163	1.062	0.736	17.327
6	22.149	1.062	0.7	16.474
7	21.865	1.045	0.717	16.39
8	22.058	1.061	0.699	16.368
9	20.886	1.058	0.723	15.977
10	22.13	1.059	0.686	16.073
11	21.792	1.062	0.731	16.901
12	21.246	1.063	0.735	16.597
13	20.345	1.061	0.725	15.655
14	21.429	1.062	0.731	16.629
15	21.667	1.061	0.73	16.785
16	20.894	1.057	0.712	15.718
17	22.463	1.066	0.705	16.883
18	22.336	1.063	0.706	16.766
19	21.117	1.06	0.737	16.493
20	20.356	1.062	0.727	15.719
Average	21.592 ±0.637	1.059 ±0.005	0.718 ±0.014	16.409 ±0.447

Tab. S2. Photovoltaic parameters for twenty perovskite solar cells based on the TiO_2 electronic transport layer. Average Jsc, Voc, FF and PCE were 20.868 $mA \cdot cm^{-2}$, 1.051 V, 0.686 and 15.042%, respectively.

Device #	J_{sc} (mA·cm^{-2})	V_{oc} (V)	FF	PCE (%)
1	20.993	1.053	0.686	15.168
2	20.034	1.041	0.676	14.108
3	19.514	1.051	0.687	14.098
4	21.793	1.057	0.67	15.426
5	21.602	1.055	0.677	15.441
6	22.639	1.031	0.64	14.95
7	21.923	1.041	0.629	14.342
8	22.089	1.035	0.683	15.625
9	20.716	1.048	0.669	14.517
10	20.136	1.059	0.729	15.562
11	21.51	1.042	0.682	15.278
12	21.564	1.056	0.685	15.59
13	20.072	1.06	0.732	15.578
14	20.145	1.06	0.731	15.611
15	21.27	1.056	0.679	15.261
16	19.633	1.041	0.694	14.185
17	21.648	1.052	0.695	15.823
18	20.368	1.057	0.723	15.562
19	20.17	1.059	0.69	14.739
20	20.328	1.066	0.681	14.761
Average	20.868 ±0.883	1.051 ±0.009	0.686 ±0.026	15.042 ±0.559